# Supporting Information

## Zero Thermal Expansion in $ZrMgMo_3O_{12}$: NMR Crystallography Reveals Origins of Thermoelastic Properties

Carl P. Romao,[1] Frédéric A. Perras,[2] Ulrike Werner-Zwanziger,[1] Joey A. Lussier,[3] Kimberly J. Miller,[1] Courtney M. Calahoo,[1] Josef W. Zwanziger,[1,4] Mario Bieringer,[3] Bojan A. Marinkovic,[5] David L. Bryce[2] and Mary Anne White[1,4,*]

[1] Department of Chemistry, Dalhousie University, Halifax B3H 4R2, Nova Scotia, Canada

[2] Department of Chemistry, University of Ottawa, Ottawa K1N 6N5, Ontario, Canada

[3] Department of Chemistry, University of Manitoba, Winnipeg R3T 2N2, Manitoba, Canada

[4] Institute for Research in Materials, Dalhousie University, Nova Scotia B3H 4R2, Halifax, Canada

[5] Departamento de Engenharia de Materiais, Pontifícia Universidade Católica de Rio de Janeiro – PUC-Rio, Rua Marquês de São Vicente 225, Gávea, Rio de Janeiro, RJ, Brasil

[*] Author for correspondence; email: mawhite@dal.ca

**Table of Contents**

## I. Methods

Table S1: A summary of different experimental measurements reported in this work and the temperature ranges in which they were performed.

| Method | Used to determine: | Temperature range / °C | $\alpha_\ell$ / $K^{-1}$ | See Figure: |
|---|---|---|---|---|
| DSC | Phase transition temp. | −175 to 35 | - | S3 |
| TGA | Decomposition temp. | 28 to 900 | - | S4 |
| Dilatometry | CTE | 23 to 500 | $4.1 \times 10^{-7}$ | 1 |
| Dilatometry | CTE | 30 to 600 | $-1 \times 10^{-8}$ | S6 |
| Dilatometry | CTE | 30 to 700 | $9 \times 10^{-7}$ | S6 |
| Dilatometry | CTE | 30 to 700 | $4 \times 10^{-7}$ | S6 |
| Dilatometry | CTE | 30 to 500 | $-2 \times 10^{-6}$ | S7 |
| Dilatometry | CTE | 30 to 500 | $-1 \times 10^{-6}$ | S7 |
| Dilatometry | CTE | 30 to 400 | $-5 \times 10^{-7}$ | S7 |
| VT-XRD | CTE | 25 to 450 | $1.7 \times 10^{-7}$ | 2, 3 |
| VT-XRD | CTE | 25 to 450 | $1.5 \times 10^{-7}$ | 2, 3 |
| VT-XRD | CTE | 450 to 650 | $9 \times 10^{-7}$ | 2, 3 |
| VT-XRD | CTE | 450 to 650 | $1 \times 10^{-6}$ | 2, 3 |
| VT-XRD | CTE | 25 to 450 | $6.8 \times 10^{-7}$ | S10 |
| Velocity of sound | Elastic constants | RT | - | - |
| XRD | Structure | RT | - | S12 |
| $^{95}$Mo NMR | Structure | RT | - | 3 |
| $^{91}$Zr NMR | Structure | RT | - | 3 |
| $^{25}$Mg NMR | Structure | RT | - | 3 |
| $^{17}$O NMR | Structure validation | RT | - | 5, S15 |
| Raman spectroscopy | Phonon energies | RT | - | 6 |
| VT-impedance | Ionic conductivity | 340 to 520 | - | S17, S18 |

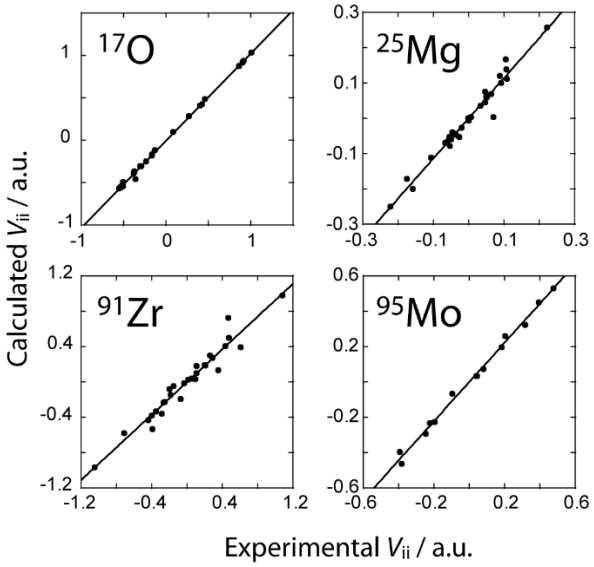


Figure S1. Calibration correlations between the PAW DFT calculated and experimentally determined EFG tensor components for all elements in $ZrMgMo_3O_{12}$.[†]

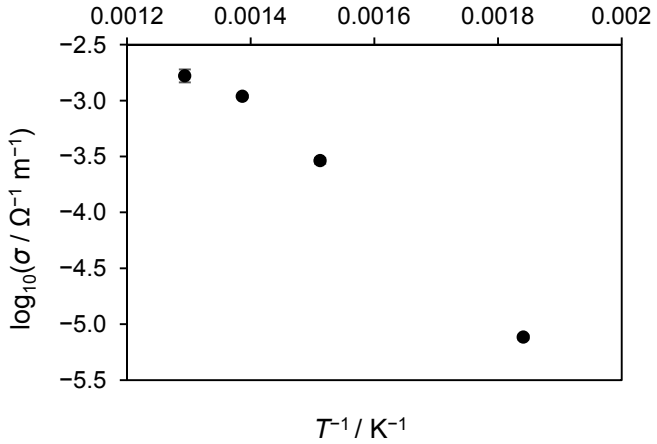


Figure S2: Ionic conductivity ($\sigma$) of $Sc_2W_3O_{12}$ (plotted on a logarithmic scale), reported here to validate the measurement apparatus (compare Imanaka, N.; Kobyashi, Y.; Tamura, S.; Adachi, G. *Solid State Ionics* **2000**, *136–137*, 319–324). Attempts to measure the conductivity of $HfMgW_3O_{12}$ for comparison with Omote, A.; Yotsuhashi, S.; Zenitani, Y.; Yamada, Y. *J. Am. Ceram. Soc.* **2011**, *94*, 2285–2288 resulted in sample decomposition as a result of application of the AC voltage.

[†] The NMR data for α- and β-$MgSO_4$, forsterite, $Mg(acac)_2$, $Mg(CH_3COO)_2$, $MgMoO_4$, $Mg(OH)_2$, MgO, $MgVO_4$, and $MgWO_4$ were used to calibrate the $^{25}$Mg EFG tensor calculations. The NMR data for $Ba_2ZrF_8$, $Cs_2ZrF_6$, $K_2ZrF_6$, monoclinic and orthorhombic $ZrO_2$, $Na_2ZrO_3$, $Na_2ZrSiO_5$, $Na_5Zr_2F_{13}$, $ZrCl_4$, $ZrI_4$, and $ZrSiO_4$ were used to calibrate the $^{91}$Zr EFG tensor calculations. The NMR data for $K_2MoO_4$, $NH_4MoO_4$ (mP60 and mS60), $PbMoO_4$, and $ZnMoO_4$ were used to calibrate the $^{95}$Mo EFG tensor calculations. The $^{17}$O calibration is from *J. Phys. Chem. C* **2012**, *116*, 19472.

## II. Phase Stability

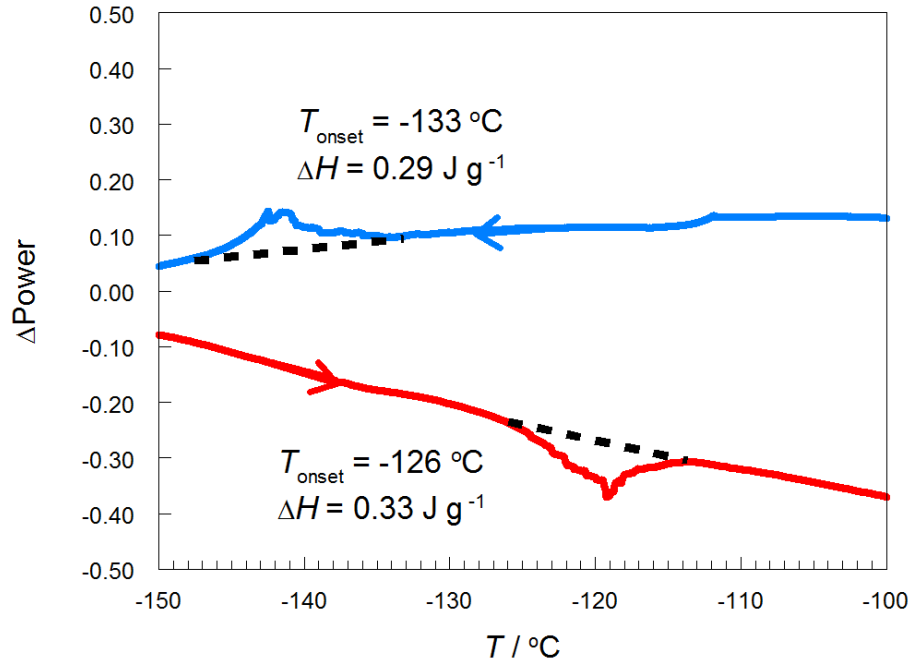


Figure S3: DSC thermogram of $ZrMgMo_3O_{12}$ (exotherm up) with cooling/heating direction, onset temperatures, peak temperatures, and transition enthalpy changes ($\Delta H$) shown. The DSC curves did not show any additional thermal events in the temperature range −160 to 30 °C.

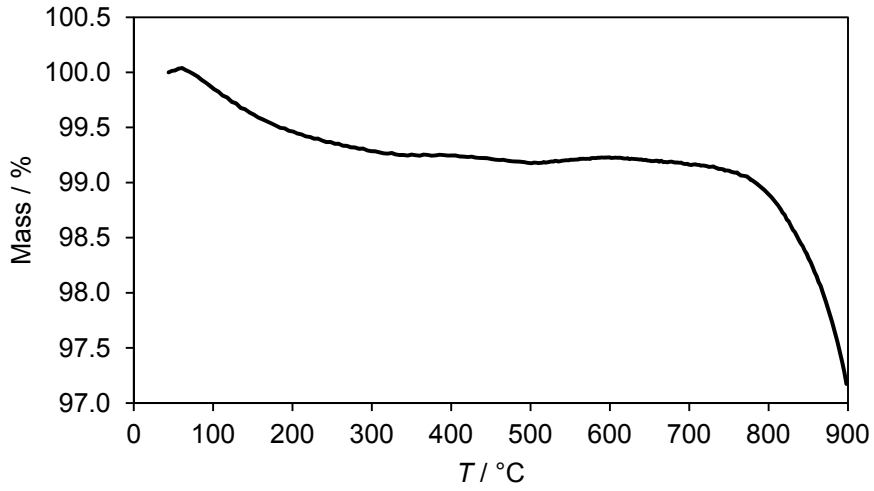


Figure S4: TGA thermogram of $ZrMgMo_3O_{12}$. Mass loss due to water from the atmosphere is very low, < 1 %, showing that it is not very hygroscopic. Decomposition into constituent oxides (followed immediately by sublimation of $MoO_3$, which is reflected in the thermogram) begins at approximately 750 °C.

## III. Thermal Expansion

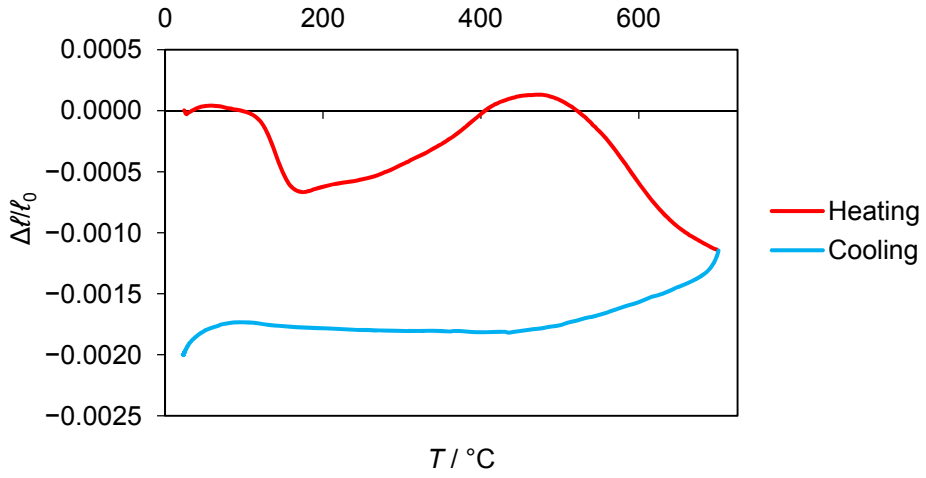


Figure S5: A dilatometric heating and cooling curve of a $ZrMgMo_3O_{12}$ sample, showing the change in length with respect to the original length as a function of temperature. "Heating" and "Cooling" refer to whether the sample temperature was being increased or decreased during the measurement. The CTE as determined via linear regression on cooling from 23 °C to 500 °C is $\alpha_\ell = 4.1 \times 10^{-7}\ K^{-1}$.

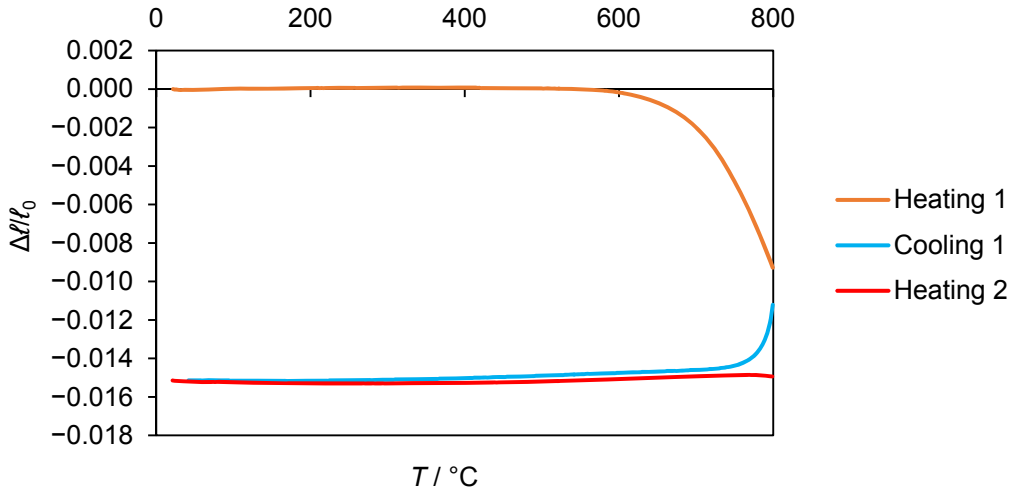


Figure S6: A dilatometric heating and cooling curve of another $ZrMgMo_3O_{12}$ sample, showing the change in length with respect to the original length as a function of temperature. "Heating 1", "Cooling 1" and "Heating 2" refer to whether the sample temperature was being increased or decreased during the measurement and whether the measurement was the first or second temperature cycle. In this case, data from the second cooling run were lost due to a power failure. The CTE was determined via linear regression from the first heating curve from 30 °C to 600 °C as $\alpha_\ell = -1 \times 10^{-8}\ K^{-1}$, from the first cooling curve from 30 °C to 700 °C as $\alpha_\ell = 9 \times 10^{-7}\ K^{-1}$ and from the second heating curve from 30 °C to 700 °C as $\alpha_\ell = 4 \times 10^{-7}\ K^{-1}$.

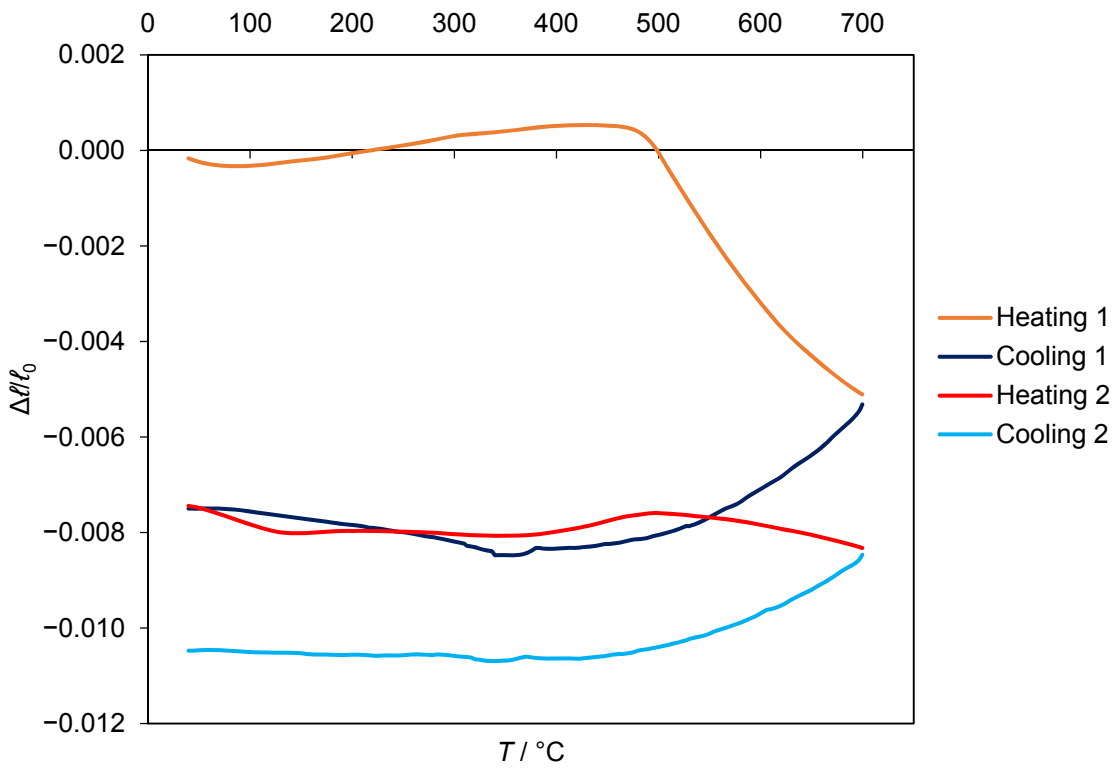


Figure S7: A dilatometric heating and cooling curve of another $ZrMgMo_3O_{12}$ sample, showing the change in length with respect to the original length as a function of temperature. “Heating 1”, “Cooling 1”, etc. refer to whether the sample temperature was being increased or decreased during the measurement and whether the measurement was the first or second temperature cycle. The measurement was considerably affected by microcrack healing and formation during the first heating. The CTE was determined via linear regression from the first cooling curve from 30 °C to 500 °C as $\alpha_\ell = -2 \times 10^{-6}\ K^{-1}$, from the second heating curve as $\alpha_\ell = -1 \times 10^{-6}\ K^{-1}$ and from the second cooling curve from 30 °C to 400 °C as $\alpha_\ell = -5 \times 10^{-7}\ K^{-1}$.

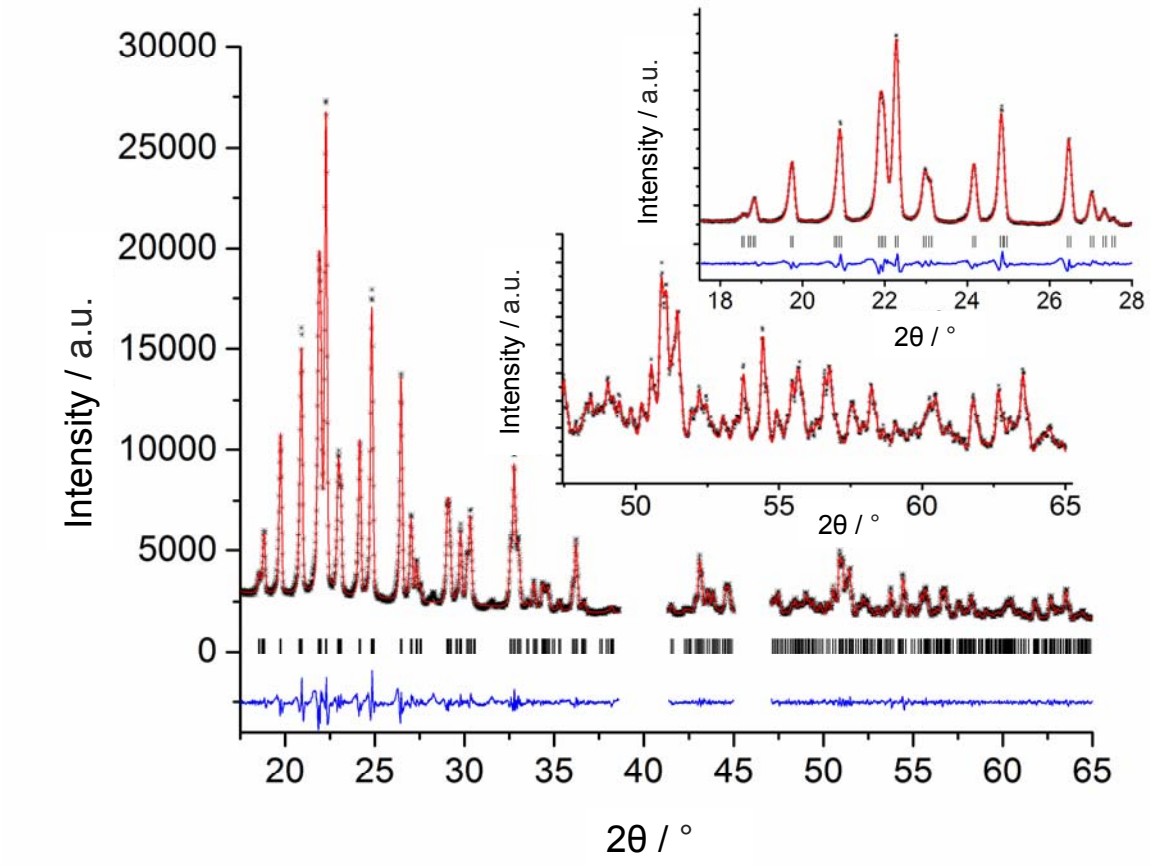


Figure S8**:** Le Bail fit for $ZrMgMo_3O_{12}$ for powder X-ray data measured at 100 °C during cooling. Black stars are experimental data; red lines are the Le Bail fit; blue lines are the difference; black bars indicate the Bragg positions.

**Axial CTEs:**

The "linear thermal expansion coefficients for the individual unit cell dimensions (axial CTEs) determined from Le Bail fits (space group: *Pna*$2_1$) of the *in-situ* powder X-ray diffraction data collected during heating in air are:

$\alpha_a$ (25°C to 450°C) = $-2.5(2) \times 10^{-6}$ $K^{-1}$
$\alpha_b$ (25°C to 450°C) = $-4.7(2) \times 10^{-6}$ $K^{-1}$
$\alpha_c$ (25°C to 450°C) = $7.6(2) \times 10^{-6}$ $K^{-1}$
➔ $\alpha_\ell$ (25°C to 450°C) = $1(2) \times 10^{-7}$ $K^{-1}$

$\alpha_a$ (475°C to 650°C) = $-0.5(2) \times 10^{-6}$ $K^{-1}$
$\alpha_b$ (475°C to 650°C) = $-2.5(2) \times 10^{-6}$ $K^{-1}$

$\alpha_c$ (475°C to 650°C) = 5.8(2) × $10^{-6}$ $K^{-1}$
➔ $\alpha_\ell$ (475°C to 50°C) = 9(2) × $10^{-7}$ $K^{-1}$)

At low temperatures (25°C to 450 °C) the positive $\alpha_c$ is compensated for with large negative $\alpha_a$ and $\alpha_b$ values resulting in almost zero expansion as expressed with a very small $\alpha_\ell$ value. At higher temperatures (475°C to 650 °C) the still fairly large positive $\alpha_c$ value is not compensated for because the $\alpha_a$ and $\alpha_b$ values are now less negative and thus a larger positive $\alpha_\ell$ value results.

**Note:** The unit cell dimensions do not change linearly with temperature. However to determine CTEs we fitted the data linearly and computed $\alpha_\ell$ values from those linear fits. Consequently the uncertainties are larger than those for the original values computed using the volume expansion. The linear fits for the individual unit cell dimension changes are shown in Figure S9. The thermal expansion of the unit cell axes was fit by two linear segments (from 25°C to 450 °C and from 475°C to 650 °C), although there is no discontinuity at 450 °C.

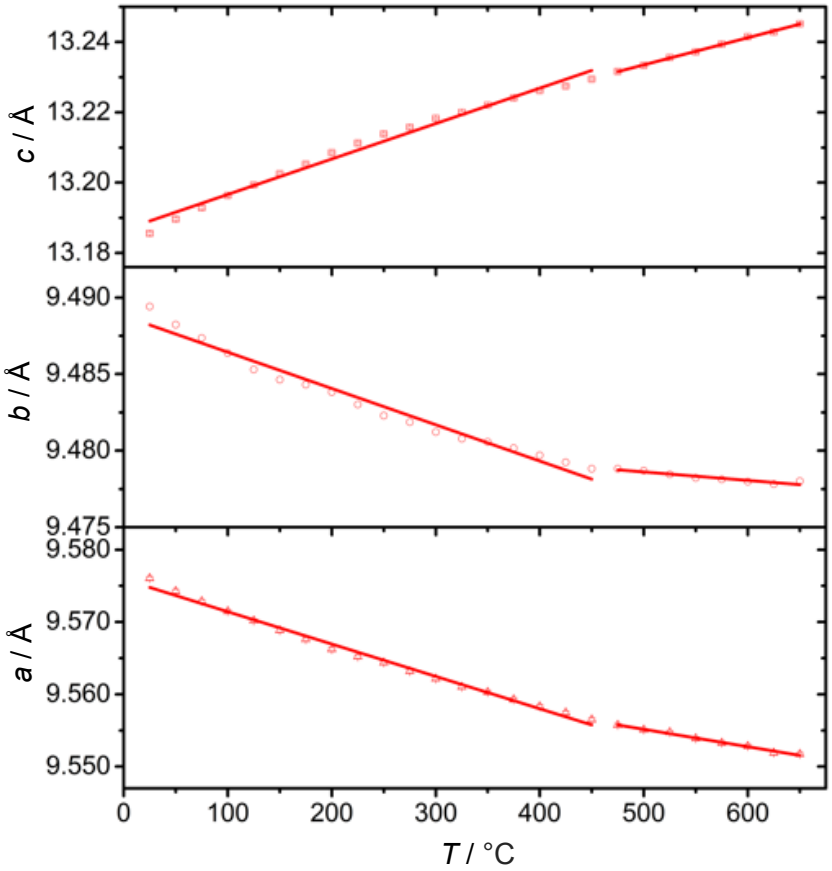


Figure S9: Unit cell dimension evolution as a function of temperature as determined by *in-situ* powder X-ray diffraction during heating in air. Red symbols = heating, red lines = linear fits of heating data.

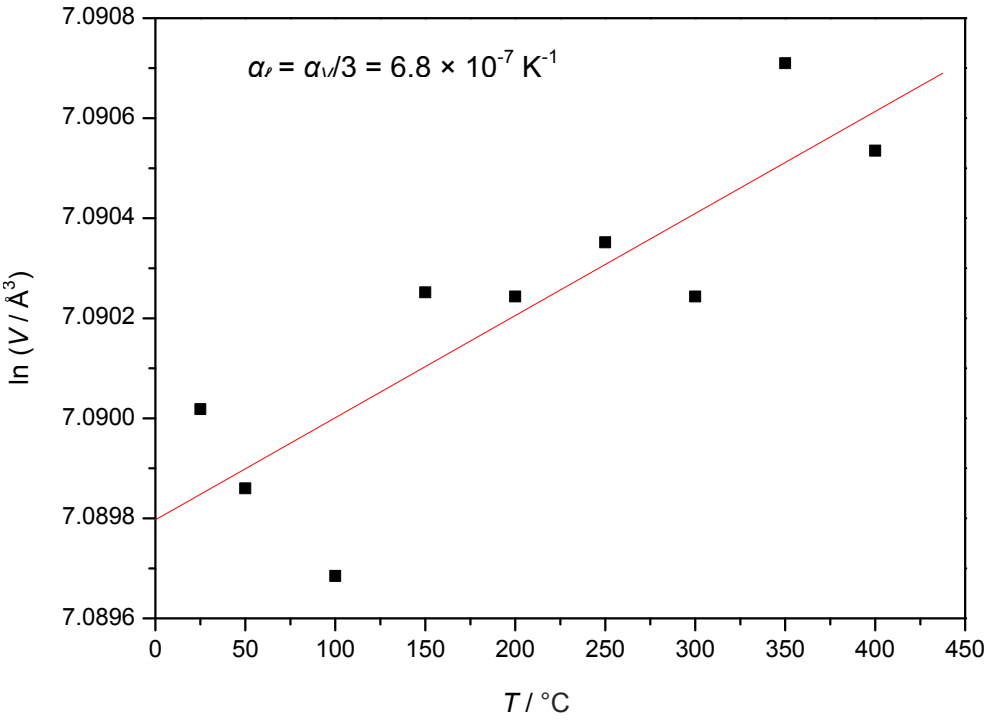


Figure S10: Linear CTE of a separately-synthesized sample of $ZrMgMo_3O_{12}$, calculated based on Le Bail fits of XRPD patterns taken at 25, 50, 100, 150, 200, 250, 300, 350 and 400 °C (D8 Advance equipped with XRK 900 Anton-Paar chamber). Air atmosphere.

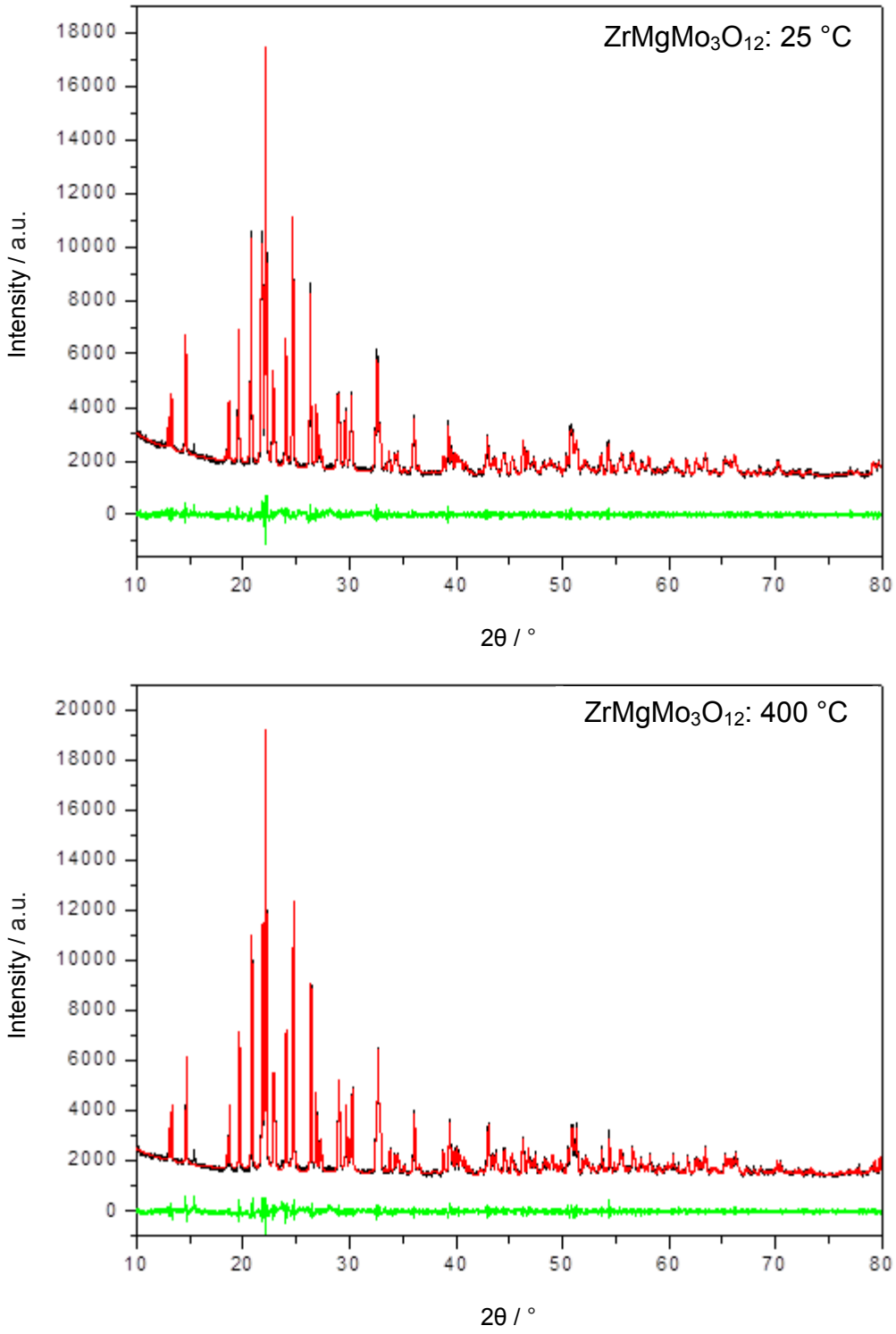


Figure S11: Example Le Bail fits of XRPD patterns used as data points in Figure S10 above.

## IV. Structure Determination by NMR Crystallography

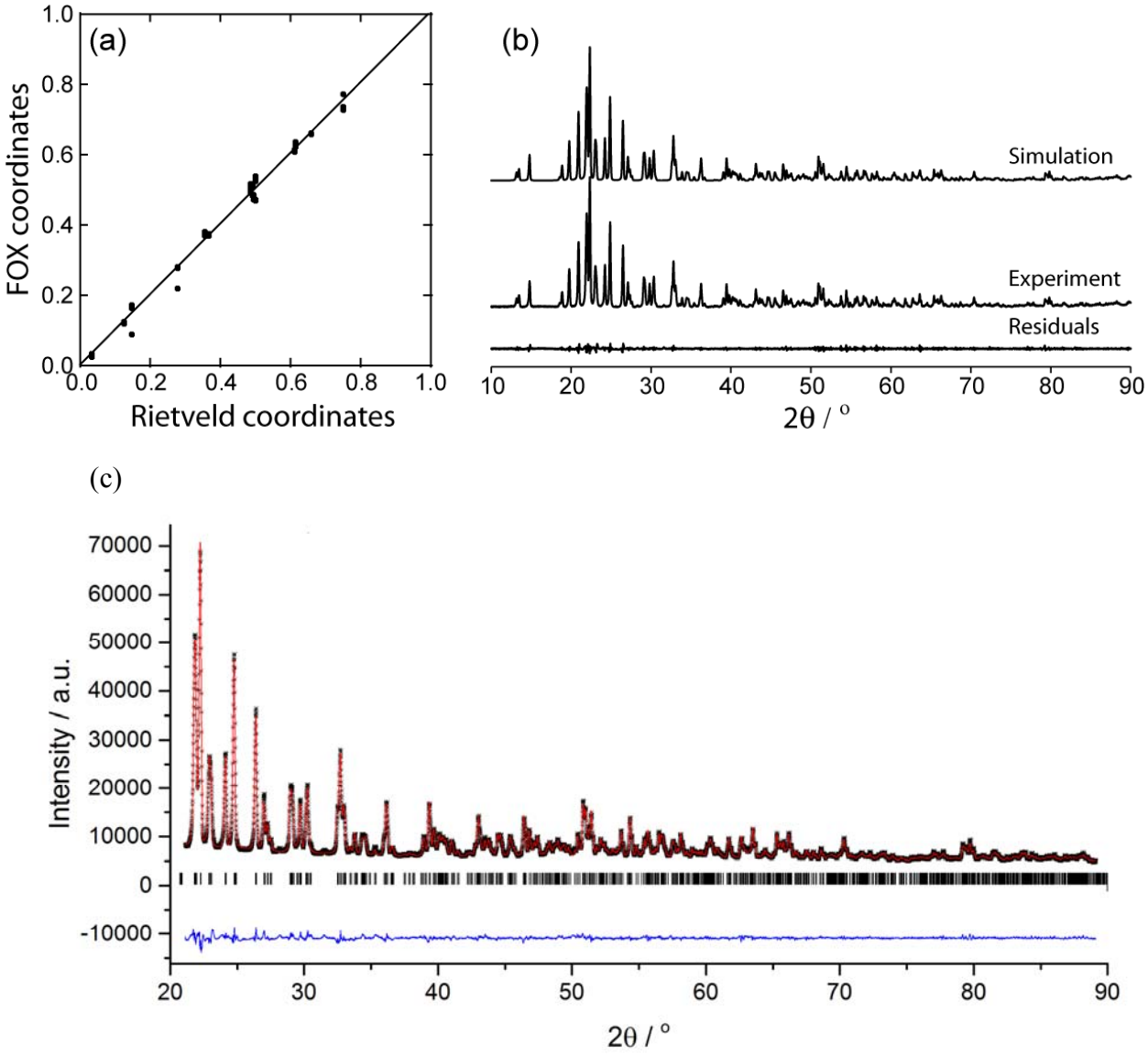


Figure S12. (a) Correlation between the fractional coordinates of the metal nuclei that were calculated with five independent FOX runs and the Rietveld-refined coordinates. (b) Graphs showing the powder X-ray diffraction pattern as well as the predicted pattern from the initial Rietveld-refined crystal structure and the residuals. (c) Rietveld plot of follow-up refinement of the $ZrMgMo_3O_{12}$ structure using the NMR derived coordinates and only refining the cation positions against X-ray data. (red = experimental data, black = best fit, blue = difference, markers indicate Bragg positions.)

Table S2. NMR parameters for all the sites in the crystal structure of $ZrMgMo_3O_{12}$.

| Site | $\delta_{iso}$[a] / ppm | $\lvert C_Q \rvert$[a,b] / MHz | $\eta$[a] |
|---|---|---|---|
| Mg | −17.4 ± 0.5 | 0.80 ± 0.05 | 0.7 ± 0.1 |
| Zr | −1 ± 5 | 5.3 ± 0.2 | 0.55 ± 0.05 |
| Mo1 | −241.0 ± 0.5 | 1.00 ± 0.05 | 1.0 ± 0.1 |
| Mo2 | −240.8 ± 0.5 | 0.92 ± 0.05 | 0.4 ± 0.1 |
| Mo3 | −250.7 ± 0.5 | 0.85 ± 0.05 | 0.63 ± 0.1 |
| O1, O6, O7 | 653.52 ± 0.03 | 1.3 ± 0.1 | -- |
| O4 | 645.4 ± 0.4 | 1.3 ± 0.5 | -- |
| O8, O10 | 638.39 ± 0.04 | 1.3 ± 0.2 | -- |
| O11 | 503.4 ± 0.2 | 1.8 ± 0.4 | -- |
| O5, O9 | 493.1 ± 0.3 | 2.0 ± 0.5 | -- |
| O2, O12 | 483.1 ± 0.1 | 1.9 ± 0.3 | -- |
| O3 | 473.40 ± 0.2 | 1.8 ± 0.4 | -- |

[a] $\delta_{iso}$ corresponds to the isotropic chemical shift, $C_Q$ is the quadrupolar coupling constant, defined as $eV_{33}Q/h$ where $e$ is the fundamental charge, $V_{33}$ is the largest EFG tensor component, $Q$ is the electric quadrupole moment of the nucleus, and $h$ is Planck's constant. $\eta$ is the asymmetry parameter of the EFG tensor, defined as $(V_{11}-V_{22})/V_{33}$, and ranges from 0 to 1.

[b] Note that this value corresponds to the quadrupolar product ($P_Q = C_Q(1+\eta^2/3)^{1/2}$) for the oxygen sites as the value of $\eta$ could not be determined.

Table S3. Cost functions ($\chi^2$) and RMSD of the various model structures from the NMR-refined crystal structure.

| Structure | $\chi^2$ | RMSD / Å |
|---|---|---|
| FOX structure | $2.04\times10^{12}$ | 0.5 ± 0.2 |
| Rietveld-refined (initial) | $1.21\times10^{12}$ | 0.24 |
| Rietveld-refined (follow-up) | $8.08\times10^{8}$ | 0.029 (cations only) |
| DFT-refined | 934.5 | 0.0014 |
| NMR-refined | 613.1 | 0 |

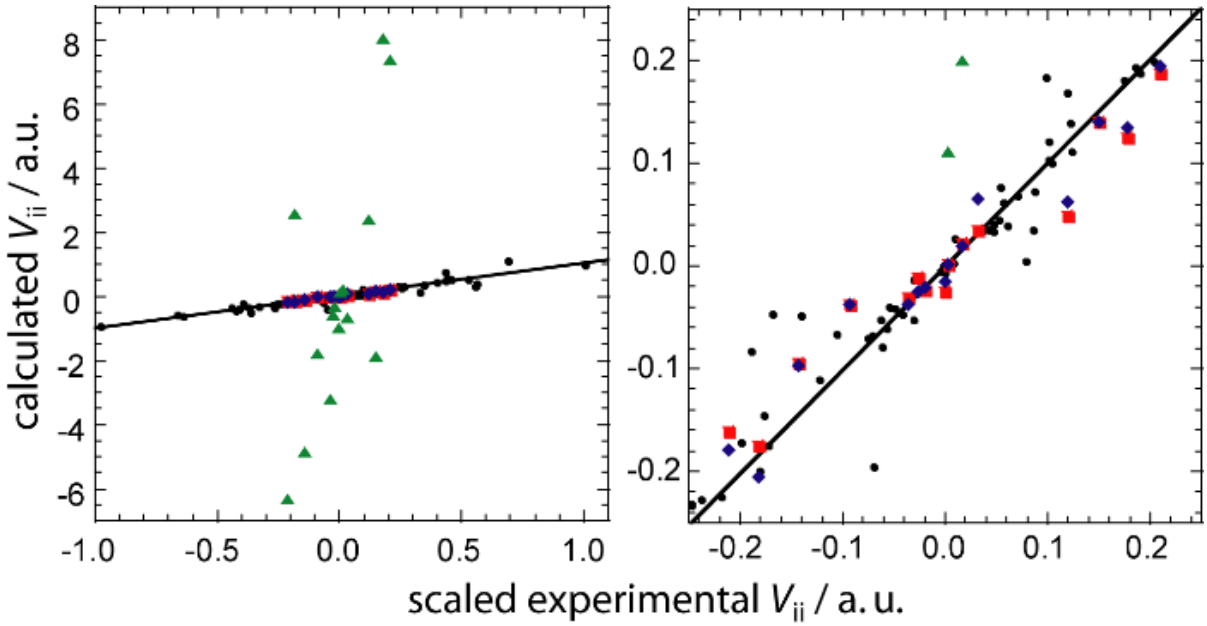


Figure S13. Correlations of the calculated EFG tensor components with the appropriately scaled experimental EFG tensor components for all metal nuclei in $ZrMgMo_3O_{12}$. The calibration data are shown as black circles, the data calculated using the Rietveld-refined structure are shown as green triangles, the data calculated using the DFT-refined structure are shown as red triangles and the data from the NMR-refined structure are shown as blue diamonds.

Table S4. Fractional coordinates for the atoms in the NMR-refined structure of $ZrMgMo_3O_{12}$, at room temperature.

| Atom | *x* | *y* | *z* | Multiplicity and Wyckoff letter |
|---|---|---|---|---|
| Zr1 | 0.0361 | 0.4975 | 0.6156 | 4a |
| Mg1 | 0.4628 | 0.5000 | 0.3732 | 4a |
| Mo1 | 0.7485 | 0.2766 | 0.4844 | 4a |
| Mo2 | 0.1303 | 0.6607 | 0.3510 | 4a |
| Mo3 | 0.6105 | 0.3623 | 0.1410 | 4a |
| O1 | 0.1065 | 0.8418 | 0.3548 | 4a |
| O2 | 0.8772 | 0.3912 | 0.5407 | 4a |
| O3 | 0.0227 | 0.5846 | 0.2526 | 4a |
| O4 | 0.3243 | 0.3357 | 0.3961 | 4a |
| O5 | 0.0870 | 0.5858 | 0.4722 | 4a |
| O6 | 0.3052 | 0.6306 | 0.3248 | 4a |
| O7 | 0.4953 | 0.4392 | 0.2260 | 4a |
| O8 | 0.5756 | 0.4293 | 0.0207 | 4a |
| O9 | 0.1691 | 0.3277 | 0.5829 | 4a |
| O10 | 0.6206 | 0.3740 | 0.4238 | 4a |
| O11 | 0.2116 | 0.5984 | 0.6752 | 4a |
| O12 | -0.0857 | 0.6742 | 0.6410 | 4a |

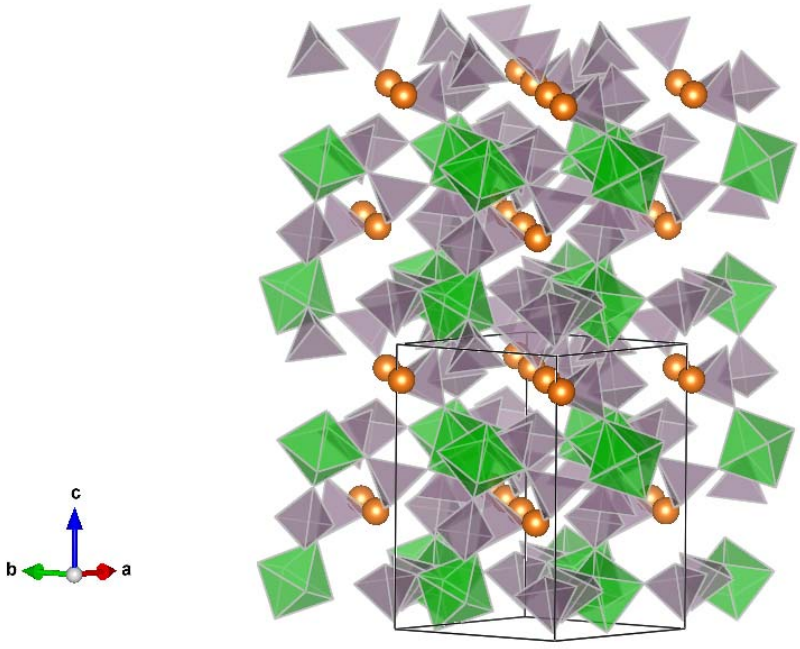


Figure S14: The NMR-refined structure of $ZrMgMo_3O_{12}$, with $Mg^{2+}$ cations shown as orange spheres, $MoO_4$ tetrahedra shown in purple and $ZrO_6$ octahedra shown in green.

## V. Structure Validation by $^{17}O$ NMR

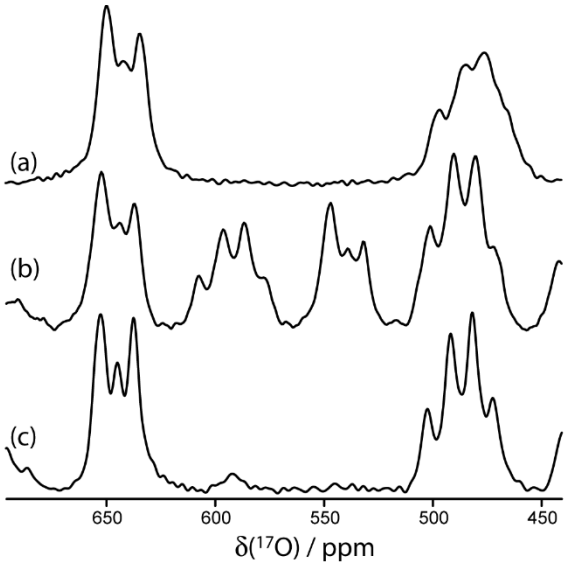


Figure S15: $^{17}O$ MAS NMR spectra acquired at applied magnetic fields of (a) 9.4 T, (b) 16.4 T, and (c) 21.1 T. (The two central features in (b) are caused by spinning sidebands.)

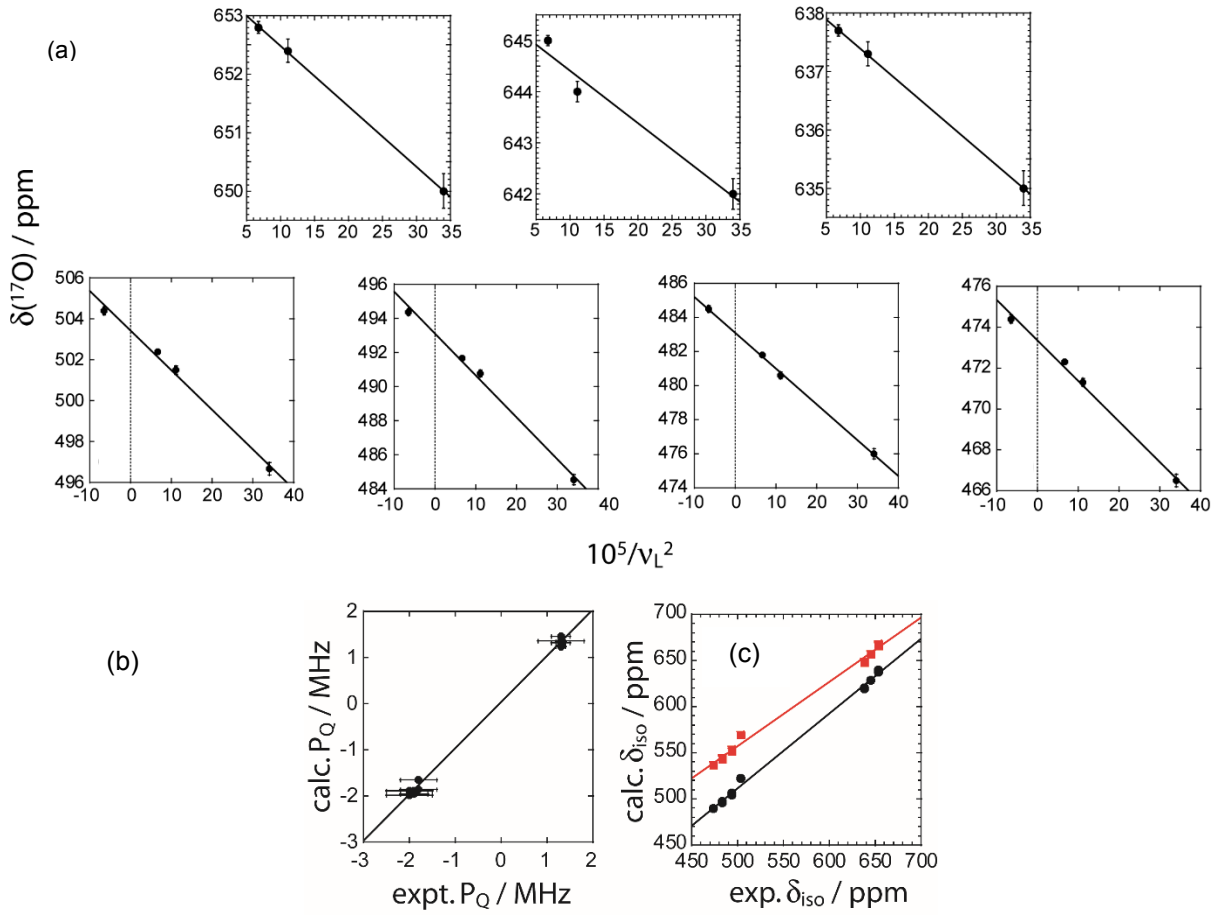


Figure S16: (a) Correlations of the apparent $^{17}O$ shifts as a function of the inverse of the squared Larmor frequency; the MQMAS data were included by scaling the value of $1/\nu_L^2$ by −10/17. (b) Correlations between the calculated and experimental $P_Q$ and (c) $\delta_{iso}$ (c) values are also shown. In (c) the red squares correspond to the GIPAW DFT calculated data whereas the black circles show the calculated shifts which were adjusted to include an *ad hoc* relativistic correction (see main text).

## VI. Phonon Modes

Table S5. Calculated Γ-point Vibrational Frequencies of $ZrMgMo_3O_{12}$.

| $\nu$ / $cm^{-1}$ | | | | | | | | | |
|---|---|---|---|---|---|---|---|---|---|
| 21.11 | 85.72 | 124.79 | 185.07 | 244.21 | 280.04 | 349.56 | 426.46 | 894.35 | 994.62 |
| 22.51 | 85.98 | 126.00 | 187.69 | 245.69 | 281.49 | 352.80 | 431.13 | 904.87 | 994.99 |
| 29.17 | 87.20 | 131.82 | 192.75 | 245.98 | 285.84 | 357.86 | 451.05 | 909.10 | 998.10 |
| 36.08 | 89.65 | 133.93 | 196.71 | 250.67 | 288.98 | 361.79 | 461.32 | 909.30 | 998.17 |
| 38.08 | 91.21 | 135.54 | 198.74 | 250.87 | 293.07 | 363.04 | 462.26 | 909.72 | 1009.41 |
| 42.77 | 91.78 | 136.71 | 201.31 | 252.54 | 293.59 | 367.22 | 462.44 | 928.91 | 1016.12 |
| 48.66 | 93.06 | 141.09 | 214.02 | 254.71 | 294.27 | 374.23 | 812.68 | 929.57 | 1023.06 |
| 50.04 | 96.62 | 142.12 | 218.01 | 254.87 | 294.80 | 390.93 | 813.83 | 935.61 | 1026.19 |
| 52.77 | 96.98 | 145.43 | 218.38 | 256.20 | 301.93 | 391.17 | 816.34 | 951.45 | 1027.11 |
| 53.87 | 98.38 | 152.10 | 219.61 | 257.70 | 302.19 | 393.24 | 817.64 | 952.06 | 1031.22 |
| 55.17 | 98.46 | 152.87 | 222.43 | 259.11 | 308.46 | 393.45 | 823.75 | 952.47 | 1031.75 |
| 57.28 | 101.13 | 157.98 | 223.97 | 260.80 | 313.40 | 398.34 | 824.52 | 957.75 | 1033.45 |
| 63.20 | 104.38 | 161.67 | 225.03 | 262.06 | 319.62 | 400.21 | 841.86 | 963.95 | |
| 63.63 | 106.09 | 163.87 | 227.36 | 265.03 | 321.25 | 402.92 | 845.09 | 966.59 | |
| 67.81 | 109.44 | 164.41 | 227.81 | 266.65 | 323.86 | 403.75 | 847.13 | 978.80 | |
| 72.42 | 113.19 | 166.88 | 230.26 | 267.62 | 324.36 | 419.38 | 871.47 | 988.59 | |
| 76.20 | 113.51 | 178.92 | 230.73 | 270.74 | 327.31 | 419.49 | 873.03 | 989.59 | |
| 78.10 | 115.88 | 179.36 | 235.77 | 271.60 | 335.10 | 420.41 | 882.56 | 991.17 | |
| 78.48 | 117.41 | 182.47 | 239.18 | 274.03 | 335.24 | 420.69 | 884.06 | 992.47 | |
| 81.14 | 119.01 | 182.74 | 240.82 | 278.31 | 337.62 | 424.69 | 889.14 | 993.05 | |
| 85.71 | 120.17 | 184.46 | 241.16 | 279.50 | 348.75 | 425.71 | 891.22 | 994.54 | |

## VII. Conductivity

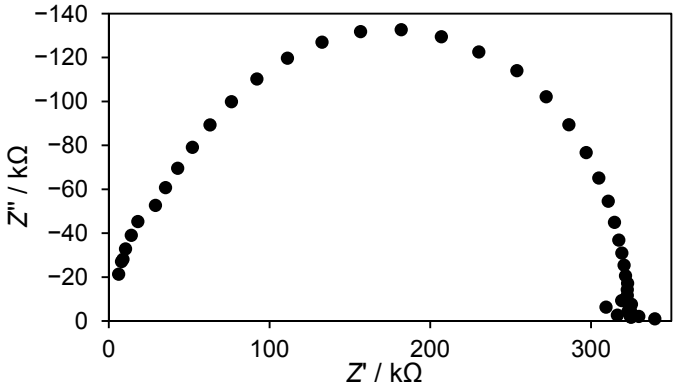


Figure S17: Nyquist plot of the real ($Z'$) and imaginary ($Z''$) components of the impedance of $ZrMgMo_3O_{12}$, measured at 400 °C.

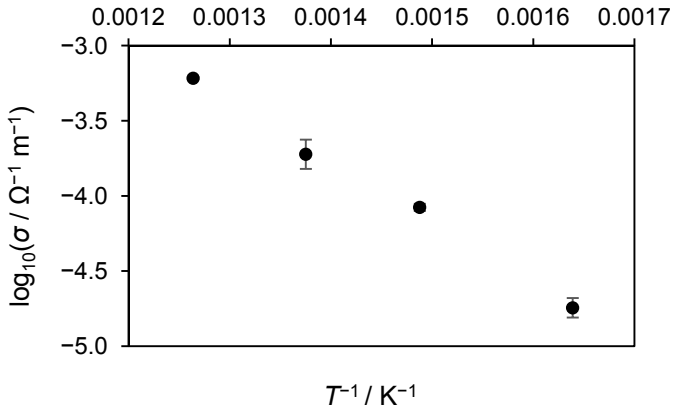


(a)

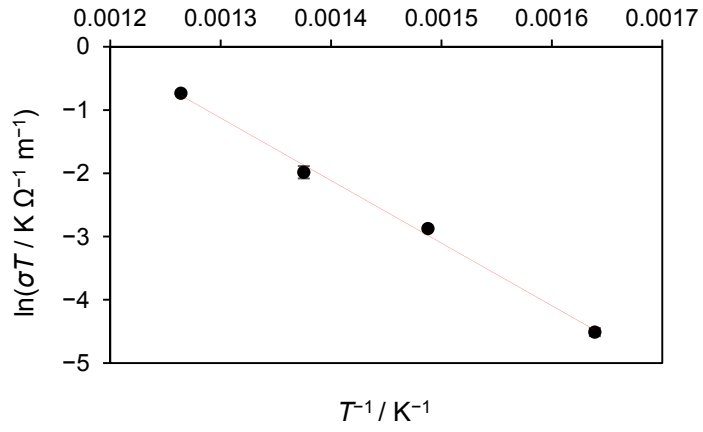


(b)

Figure S18: Ionic conductivity, $\sigma$, of $ZrMgMo_3O_{12}$ (a) plotted on a logarithmic scale and (b) as $\ln(\sigma T)$. The correlation coefficient relating $\ln(\sigma)$ to $T^{-1}$ is smaller than that relating $\ln(\sigma T)$ to $T^{-1}$ (0.9959 *vs*. 0.9965), supporting the assertion that conductivity in $ZrMgMo_3O_{12}$ is ionic. The derivative of $\ln(\sigma T)$ with respect to $T^{-1}$ is equal to the activation energy (82 kJ $mol^{-1}$) divided by the gas constant, $R$.

## VIII. Correlation of Structure and Properties

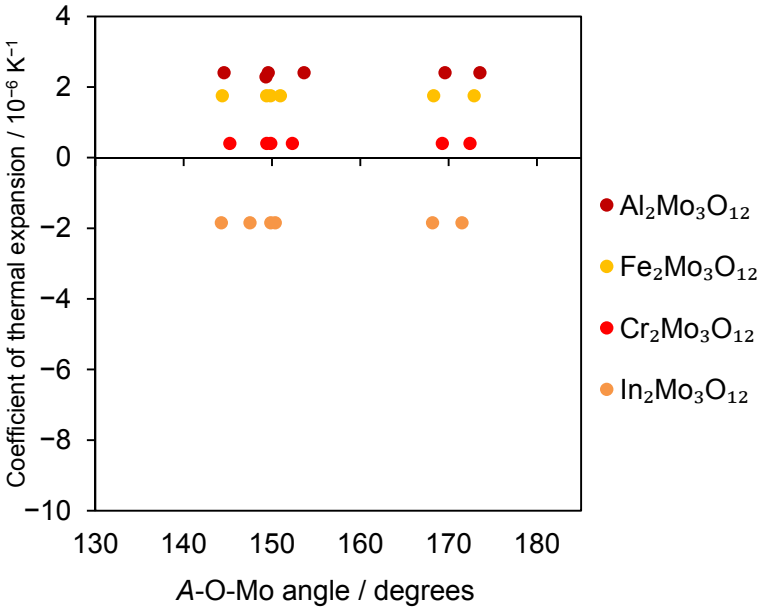


(a)

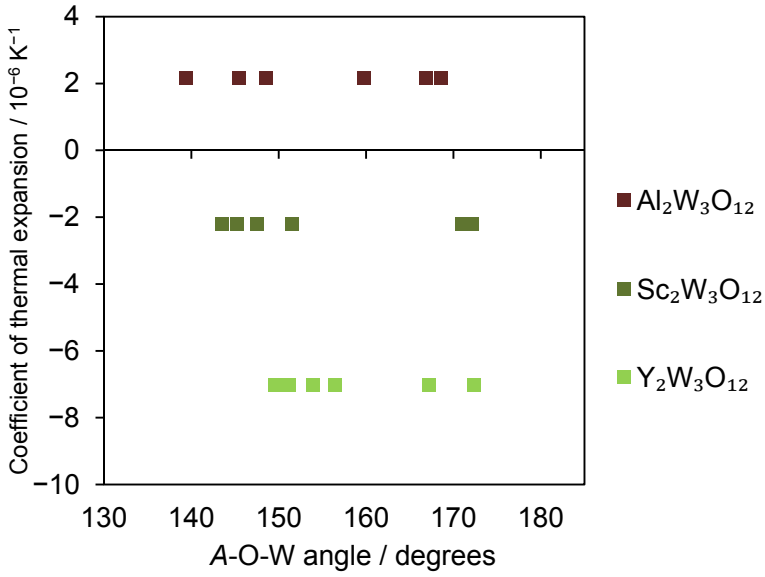


(b)

Figure S19: Correlation of CTE in the orthorhombic phase of $A_2Mo_3O_{12}$ materials with *M*-O-*A*/Mg bond angles for (a) $A_2Mo_3O_{12}$ materials which undergo a phase transition into their orthorhombic phase above room temperature, and (b) $A_2W_3O_{12}$ materials (all of which are stable in an orthorhombic phase at room temperature). Information for $A_2M_3O_{12}$ materials was taken from the literature; see Table 1 for references.

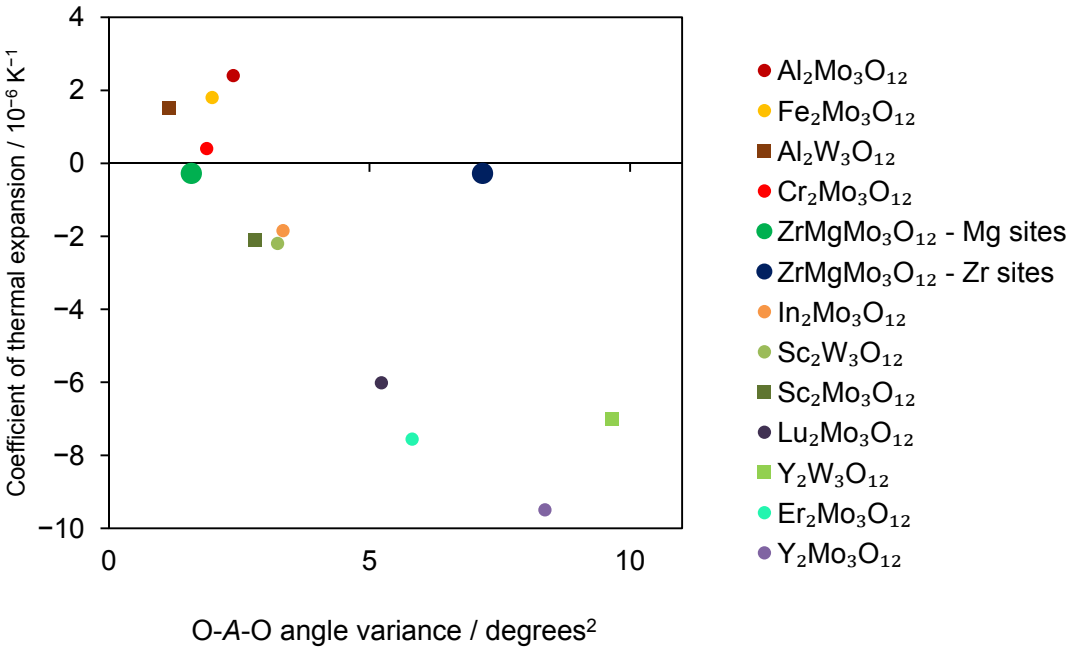
Coefficient of thermal expansion / 10⁻⁶ K⁻¹
4
2
0
−2
−4
−6
−8
−10
0
5
10
O-A-O angle variance / degrees²
Al2Mo3O12
Fe2Mo3O12
Al2W3O12
Cr2Mo3O12
ZrMgMo3O12 - Mg sites
ZrMgMo3O12 - Zr sites
In2Mo3O12
Sc2W3O12
Sc2Mo3O12
Lu2Mo3O12
Y2W3O12
Er2Mo3O12
Y2Mo3O12

(a)

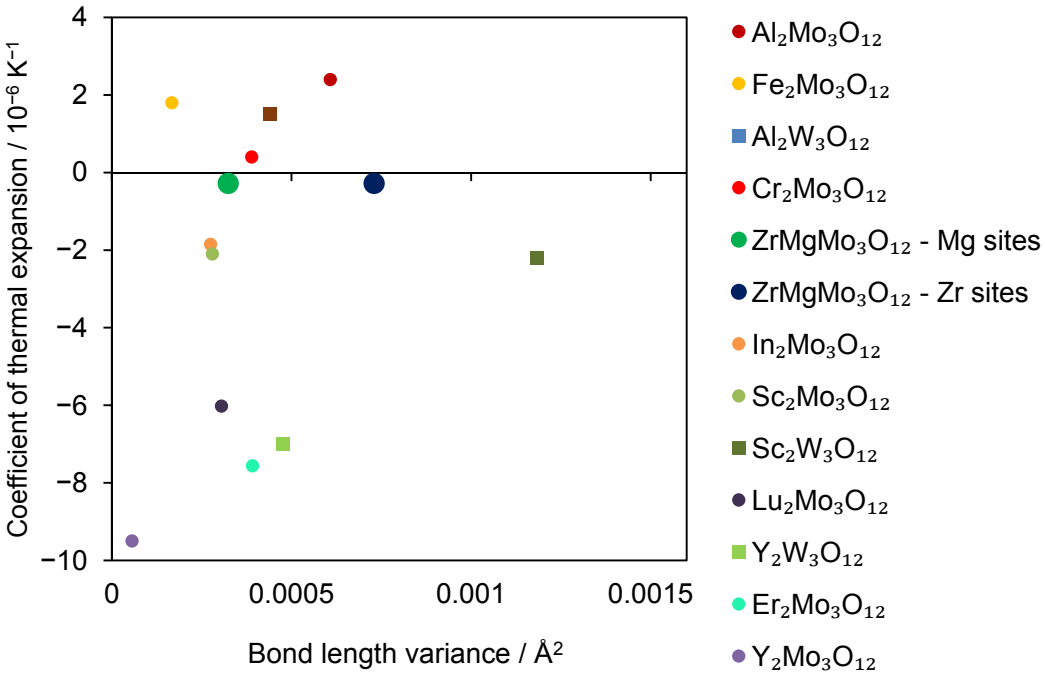
Coefficient of thermal expansion / 10⁻⁶ K⁻¹
4
2
0
−2
−4
−6
−8
−10
0
0.0005
0.001
0.0015
Bond length variance / Å²
Al2Mo3O12
Fe2Mo3O12
Al2W3O12
Cr2Mo3O12
ZrMgMo3O12 - Mg sites
ZrMgMo3O12 - Zr sites
In2Mo3O12
Sc2Mo3O12
Sc2W3O12
Lu2Mo3O12
Y2W3O12
Er2Mo3O12
Y2Mo3O12

(b)

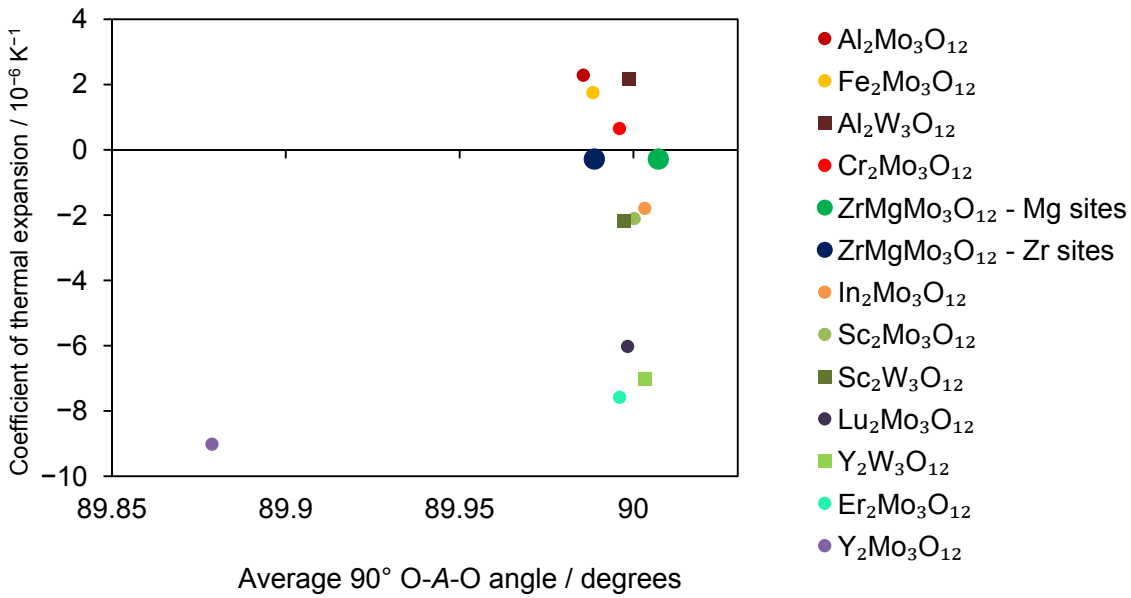


(c)

Figure S20: Coefficients of thermal expansion of $ZrMgMo_3O_{12}$ (large symbols) and $A_2M_3O_{12}$ materials compared to three causes of polyhedral distortion: (a) O-*A*-O angle variance, (b) bond length variance, and (c) the average 90° O-*A*-O angle. The O-*A*-O angle variance is the dominant contributor to the polyhedral distortion (Figure 8 (a)) except in the case of $Y_2Mo_3O_{12}$. Structural information regarding $A_2M_3O_{12}$ materials was taken from the literature; see Table 1 for references.

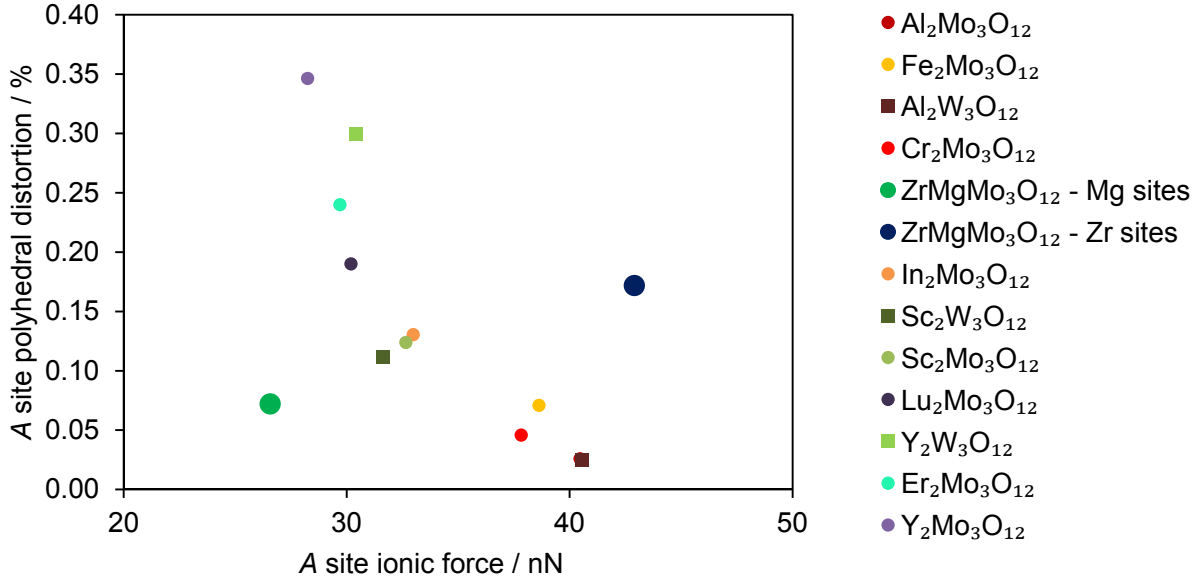


Figure S21: Inherent polyhedral distortion ($AO_6$) in $ZrMgMo_3O_{12}$ (large symbols) and $A_2M_3O_{12}$ materials as a function of their *A* site ionic force. Structural information for $A_2M_3O_{12}$ materials was taken from the literature; see Table 1 for references.

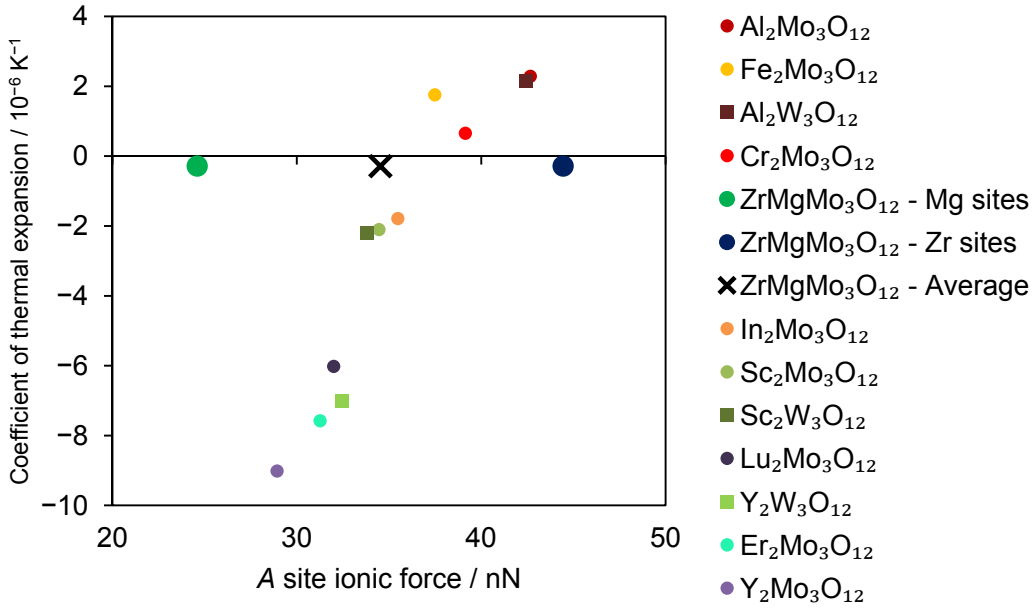


Figure S22: Coefficients of thermal expansion of $ZrMgMo_3O_{12}$ (large symbols) and $A_2M_3O_{12}$ materials as a function of their *A* site ionic force, calculated as a function of the *A*-O bond length rather than the sum of ionic radii. Structures of $A_2M_3O_{12}$ materials were taken from the literature; see Table 1.

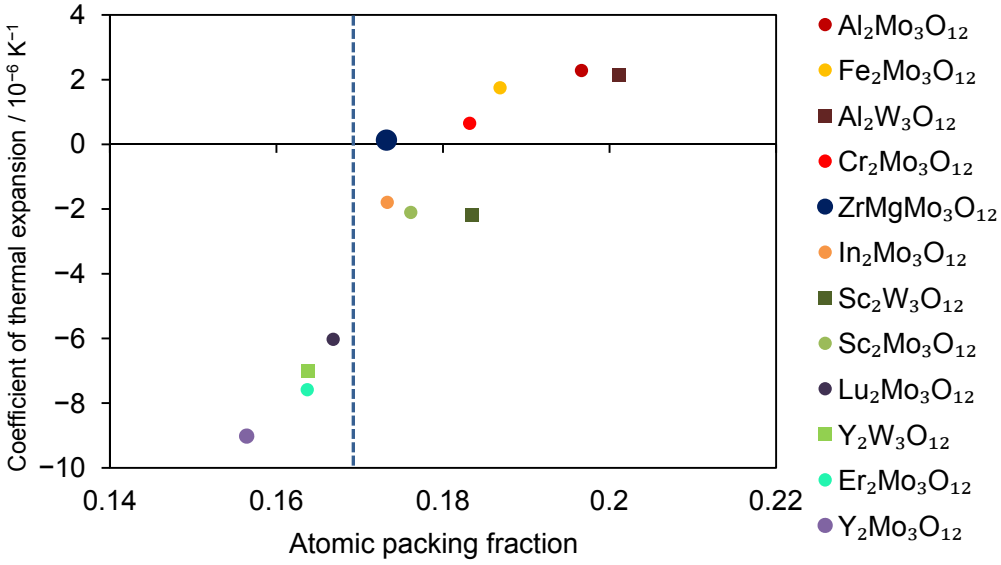


Figure S23: Atomic packing fractions of $ZrMgMo_3O_{12}$ (large symbols) shown in comparison to their coefficients of thermal expansion. The dotted blue line separates materials with significant hygroscopicity due to incorporation of crystal waters (to the left of the line) from those without this property. Structural data for $A_2M_3O_{12}$ materials were taken from the literature; see Table 1 for details.